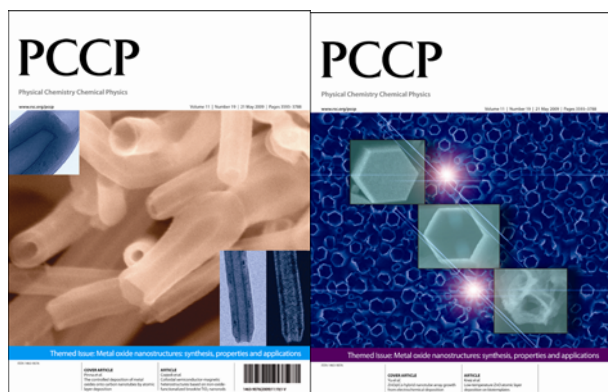


This paper is published as part of a PCCP Themed Issue on:  
[Metal oxide nanostructures: synthesis, properties and applications](#)



Guest Editors: Nicola Pinna, Markus Niederberger, John Martin Gregg and Jean-Francois Hochepeid

## Editorial

### [Chemistry and physics of metal oxide nanostructures](#)

*Phys. Chem. Chem. Phys.*, 2009

DOI: [10.1039/b905768d](#)

## Papers

### [Thermally stable ordered mesoporous CeO<sub>2</sub>/TiO<sub>2</sub> visible-light photocatalysts](#)

Guisheng Li, Dieqing Zhang and Jimmy C. Yu, *Phys. Chem. Chem. Phys.*, 2009

DOI: [10.1039/b819167k](#)

### [Blue nano titania made in diffusion flames](#)

Alexandra Teleki and Sotiris E. Pratsinis, *Phys. Chem. Chem. Phys.*, 2009

DOI: [10.1039/b821590a](#)

### [Shape control of iron oxide nanoparticles](#)

Alexey Shavel and Luis M. Liz-Marzán, *Phys. Chem. Chem. Phys.*, 2009

DOI: [10.1039/b822733k](#)

### [Colloidal semiconductor/magnetic heterostructures based on iron-oxide-functionalized brookite TiO<sub>2</sub> nanorods](#)

Raffaella Buonsanti, Etienne Snoeck, Cinzia Giannini, Fabia Gozzo, Mar Garcia-Hernandez, Miguel Angel Garcia, Roberto Cingolani and Pantaleo Davide Cozzoli, *Phys. Chem. Chem. Phys.*, 2009

DOI: [10.1039/b821964h](#)

### [Low-temperature ZnO atomic layer deposition on biotemplates: flexible photocatalytic ZnO structures from eggshell membranes](#)

Seung-Mo Lee, Gregor Grass, Gyeong-Man Kim, Christian Dresbach, Lianbing Zhang, Ulrich Gösele and Mato Knez, *Phys. Chem. Chem. Phys.*, 2009

DOI: [10.1039/b820436e](#)

### [A LEEM/ \$\mu\$ -LEED investigation of phase transformations in TiO/Pt\(111\) ultrathin films](#)

Stefano Agnoli, T. Onur Menteş, Miguel A. Niño, Andrea Locatelli and Gaetano Granozzi, *Phys. Chem. Chem. Phys.*, 2009

DOI: [10.1039/b821339a](#)

### [Synthesis and characterization of V<sub>2</sub>O<sub>5</sub> nanorods](#)

Alexander C. Santulli, Wenqian Xu, John B. Parise, Liusuo Wu, M.C. Aronson, Fen Zhang, Chang-Yong Nam, Charles T. Black, Amanda L. Tiano and Stanislaus S. Wong, *Phys. Chem. Chem. Phys.*, 2009

DOI: [10.1039/b822902c](#)

### [Flame spray-pyrolyzed vanadium oxide nanoparticles for lithium battery cathodes](#)

See-How Ng, Timothy J. Patey, Robert Büchel, Frank Krumeich, Jia-Zhao Wang, Hua-Kun Liu, Sotiris E. Pratsinis and Petr Novák, *Phys. Chem. Chem. Phys.*, 2009

DOI: [10.1039/b821389p](#)

### [Mesoporous sandwiches: towards mesoporous multilayer films of crystalline metal oxides](#)

Rainer Ostermann, Sébastien Sallard and Bernd M. Smarsly, *Phys. Chem. Chem. Phys.*, 2009

DOI: [10.1039/b820651c](#)

### [Surprisingly high, bulk liquid-like mobility of silica-confined ionic liquids](#)

Ronald Göbel, Peter Hesemann, Jens Weber, Eléonore Möller, Alwin Friedrich, Sabine Beuermann and Andreas Taubert, *Phys. Chem. Chem. Phys.*, 2009

DOI: [10.1039/b821833a](#)

### [Fabrication of highly ordered, macroporous Na<sub>2</sub>W<sub>2</sub>O<sub>7</sub> arrays by spray pyrolysis using polystyrene colloidal crystals as templates](#)

SunHyung Lee, Katsuya Teshima, Maki Fujisawa, Syuji Fujii, Morinobu Endo and Shuji Oishi, *Phys. Chem. Chem. Phys.*, 2009

DOI: [10.1039/b821209k](#)

### [Nanoporous Ni-Ce<sub>0.8</sub>Gd<sub>0.2</sub>O<sub>1.9-x</sub> thin film cermet SOFC anodes prepared by pulsed laser deposition](#)

Anna Infortuna, Ashley S. Harvey, Ulrich P. Muecke and Ludwig J. Gauckler, *Phys. Chem. Chem. Phys.*, 2009

DOI: [10.1039/b821473e](#)

### [Surface chemistry of carbon-templated mesoporous aluminas](#)

Thomas Onfroy, Wen-Cui Li, Ferdi Schüth and Helmut Knözinger, *Phys. Chem. Chem. Phys.*, 2009

DOI: [10.1039/b821505g](#)

### [ZnO@Co hybrid nanotube arrays growth from electrochemical deposition: structural, optical, photocatalytic and magnetic properties](#)

Li-Yuan Fan and Shu-Hong Yu, *Phys. Chem. Chem. Phys.*, 2009

DOI: [10.1039/b823379a](#)

### [Electrochemistry of LiMn<sub>2</sub>O<sub>4</sub> nanoparticles made by flame spray pyrolysis](#)

T. J. Patey, R. Büchel, M. Nakayama and P. Novák, *Phys. Chem. Chem. Phys.*, 2009

DOI: [10.1039/b821572n](#)

### [Ligand dynamics on the surface of zirconium oxo clusters](#)

Philip Walther, Michael Puchberger, F. Rene Kogler, Karlheinz Schwarz and Ulrich Schubert, *Phys. Chem. Chem. Phys.*, 2009

DOI: [10.1039/b820731c](#)

**[Thin-walled Er<sup>3+</sup>:Y<sub>2</sub>O<sub>3</sub> nanotubes showing up-converted fluorescence](#)**

Christoph Erk, Sofia Martin Caba, Holger Lange, Stefan Werner, Christian Thomsen, Martin Steinhart, Andreas Berger and Sabine Schlecht, *Phys. Chem. Chem. Phys.*, 2009

DOI: [10.1039/b821304f](https://doi.org/10.1039/b821304f)

**[Wettability conversion of colloidal TiO<sub>2</sub> nanocrystal thin films with UV-switchable hydrophilicity](#)**

Gianvito Caputo, Roberto Cingolani, Pantaleo Davide Cozzoli and Athanassia Athanassiou, *Phys. Chem. Chem. Phys.*, 2009

DOI: [10.1039/b823331d](https://doi.org/10.1039/b823331d)

**[Nucleation and growth of atomic layer deposition of HfO<sub>2</sub> gate dielectric layers on silicon oxide: a multiscale modelling investigation](#)**

A. Dkhissi, G. Mazaleyrat, A. Estève and M. Djafari Rouhani, *Phys. Chem. Chem. Phys.*, 2009

DOI: [10.1039/b821502b](https://doi.org/10.1039/b821502b)

**[Designing meso- and macropore architectures in hybrid organic-inorganic membranes by combining surfactant and breath figure templating \(BFT\)](#)**

Ozlem Sel, Christel Laberty-Robert, Thierry Azais and Clément

Sanchez, *Phys. Chem. Chem. Phys.*, 2009

DOI: [10.1039/b821506e](https://doi.org/10.1039/b821506e)

**[The controlled deposition of metal oxides onto carbon nanotubes by atomic layer deposition: examples and a case study on the application of V<sub>2</sub>O<sub>5</sub> coated nanotubes in gas sensing](#)**

Marc-Georg Willinger, Giovanni Neri, Anna Bonavita, Giuseppe Micali, Erwan Rauwel, Tobias Hertrich and Nicola Pinna, *Phys. Chem. Chem. Phys.*, 2009

DOI: [10.1039/b821555c](https://doi.org/10.1039/b821555c)

**[In situ investigation of molecular kinetics and particle formation of water-dispersible titania nanocrystals](#)**

G. Garnweitner and C. Grote, *Phys. Chem. Chem. Phys.*, 2009

DOI: [10.1039/b821973g](https://doi.org/10.1039/b821973g)

**[Chemoresistive sensing of light alkanes with SnO<sub>2</sub> nanocrystals: a DFT-based insight](#)**

Mauro Epifani, J. Daniel Prades, Elisabetta Comini, Albert Cirera, Pietro Siciliano, Guido Faglia and Joan R. Morante, *Phys. Chem. Chem. Phys.*, 2009

DOI: [10.1039/b820665a](https://doi.org/10.1039/b820665a)

# Synthesis and characterization of V<sub>2</sub>O<sub>3</sub> nanorods†

Alexander C. Santulli,<sup>a</sup> Wenqian Xu,<sup>b</sup> John B. Parise,<sup>ab</sup> Liusuo Wu,<sup>c</sup> M. C. Aronson,<sup>cd</sup> Fen Zhang,<sup>a</sup> Chang-Yong Nam,<sup>e</sup> Charles T. Black,<sup>e</sup> Amanda L. Tiano<sup>a</sup> and Stanislaus S. Wong<sup>\*ac</sup>

Received 19th December 2008, Accepted 16th February 2009

First published as an Advance Article on the web 12th March 2009

DOI: 10.1039/b822902c

In this work, VO<sub>2</sub> nanorods have been initially generated as reactive nanoscale precursors to their subsequent conversion to large quantities of highly crystalline V<sub>2</sub>O<sub>3</sub> with no detectable impurities. Structural changes in VO<sub>2</sub>, associated with the metallic-to-insulating transition from the monoclinic form to the rutile form, have been investigated and confirmed using X-ray diffraction and synchrotron data, showing that the structural transition is reversible and occurs at around 63 °C. When this VO<sub>2</sub> one-dimensional sample was subsequently heated to 800 °C in a reducing atmosphere, it was successfully transformed into V<sub>2</sub>O<sub>3</sub> with effective retention of its nanorod morphology. We have also collected magnetic and transport data on these systems that are comparable to bulk behavior and consistent with trends observed in previous experiments.

## Introduction

Metal oxides, in particular, represent one of the most diverse classes of materials, with important structure-related properties, including superconductivity, ferroelectricity, magnetism, colossal magnetoresistivity, conductivity and gas-sensing capabilities. It is evident that the synthesis of metal oxide nanostructures will lead to key developments in the construction of devices. For instance, metal oxides are a key component in metal oxide semiconductor field effect transistors (MOSFET), which are the basis for CMOS logic used in many computational devices.<sup>1</sup> In addition, metal oxides are increasingly being utilized in the development of novel energy sources and devices, including as photovoltaics. For example, both titanium dioxide (TiO<sub>2</sub>) and zinc oxide (ZnO) have been incorporated into dye-sensitized solar cells.<sup>2,3</sup> Finally, metal oxides have also been considered as important catalysts in key commercially relevant reactions such as the photo-splitting of water,<sup>4,5</sup> the water gas shift reaction,<sup>6,7</sup> and the production of chlorine from HCl.<sup>8</sup>

Of the family of metal oxides, vanadium oxides have been of particular focus in recent years for their diverse electronic, optoelectronic, electrochromic, and magnetic properties<sup>9</sup> with potential applications as sensors, catalysts, high-energy lithium batteries, as well as electrochemical and optical

devices.<sup>10</sup> For example, vanadium oxides have been cited for their ability to initiate the gas-phase oxidation of propane to propylene,<sup>11,12</sup> due to their interesting metal-to-insulator (M–I) transitions.<sup>13</sup> Vanadium maintains several stable oxidation states, namely V<sup>3+</sup>, V<sup>4+</sup> and V<sup>5+</sup>, which allow for the formation of many stable oxides,<sup>14,15</sup> and what makes these materials exciting are their structural transformations and accompanying electronic phase transitions. The structures of most of these phases of binary VO<sub>2+x</sub> are built up of distorted VO<sub>6</sub> octahedra which share both corners and edges<sup>16</sup> with the degree of edge sharing increasing with decreasing values of ‘x’. Specifically, in this manuscript, we are interested in VO<sub>2</sub> and V<sub>2</sub>O<sub>3</sub>, each of which exhibits a metal-to-insulator transition; in the case of V<sub>2</sub>O<sub>3</sub>, this involves an evolution from a low-temperature antiferromagnetic insulator to a high-temperature paramagnetic phase,<sup>17</sup> accompanied by a seven orders-of-magnitude jump in conductivity.<sup>18</sup> These M–I transitions can occur at different temperatures, ranging from –100 °C for V<sub>2</sub>O<sub>3</sub>,<sup>19</sup> to 68 °C for VO<sub>2</sub>.<sup>20,21</sup> Moreover, one can lower the M–I transition temperature by doping with tungsten<sup>20</sup> for VO<sub>2</sub> or with molybdenum for V<sub>2</sub>O<sub>3</sub>.<sup>22,23</sup> Conversely, the M–I transition temperature could be raised by doping with chromium, as was observed with V<sub>2</sub>O<sub>3</sub>.<sup>24</sup>

Vanadium dioxide (VO<sub>2</sub>) is of particular interest due to the fact that its Mott M–I transition temperature, occurring at 68 °C, is the closest to room temperature of any of the undoped vanadium oxides currently known and is associated with an abrupt change in resistivity (a factor of 10<sup>4</sup> to 10<sup>5</sup>). That is, at room temperature, bulk vanadium dioxide adopts a distorted P<sub>2</sub>/c monoclinic structure with insulating properties. However, when heated above the transition temperature, it is converted into a tetragonal rutile P<sub>4</sub><sub>2</sub>/mmm structure, possessing metallic properties.<sup>25,26</sup> This observation renders this material as a useful candidate in possible applications ranging from robust, near-IR optical switches (reported to switch as fast as 500 fs between the two states when excited with 50-fs laser pulses at a wavelength of 800 nm),<sup>27</sup> smart

<sup>a</sup> Department of Chemistry, State University of New York at Stony Brook, Stony Brook, NY 11794-3400.

E-mail: sswong@notes.cc.sunysb.edu, sswong@bnl.gov;

Tel: +1 (1)631 632 1703; +1 (1)631 344 3178

<sup>b</sup> Department of Geosciences, State University of New York at Stony Brook, Stony Brook, NY 11794-2100

<sup>c</sup> Condensed Matter Physics and Materials Sciences Department, Brookhaven National Laboratory, Upton, NY 11973

<sup>d</sup> Department of Physics and Astronomy, State University of New York at Stony Brook, Stony Brook, NY 11794-3800

<sup>e</sup> Center for Functional Nanomaterials, Brookhaven National Laboratory, Upton, NY 11973

† Electronic supplementary information (ESI) available: XRD data. See DOI: 10.1039/b822902c

window coatings, heat sensors, optical modulators, field effect transistors, to optical storage media.<sup>20,28–35</sup>

There are a number of existing methods for synthesizing VO<sub>2</sub> nanostructures. In terms of solution approaches, nanocrystalline VO<sub>2</sub> can be synthesized by a reduction of aqueous potassium vanadate solution with potassium borohydride around pH 4.<sup>16</sup> In addition, VO<sub>2</sub> nanorod arrays can be produced using an ethylene glycol reduction approach under hydrothermal conditions.<sup>36</sup> Using an analogous approach,<sup>10</sup> vanadium oxide nanorods measuring 40–60 nm in diameter and 1 to 2 microns in length have been successfully fabricated using a surfactant-assisted hydrothermal method at 180 °C for 48 h. Moreover, with a similar methodology, precursor oxides have been mixed with either hexadecylamine or dodecylamine along with cetyltrimethyl ammonium bromide for 48 h in air followed by hydrothermal treatment at 180 °C for 1 week to generate vanadium oxide nanotubes.<sup>37–44</sup>

In terms of gas-phase protocols, VO<sub>2</sub> nanorods have been fabricated by sputtering of a vanadium-metal thin film.<sup>45</sup> In addition, VO<sub>2</sub> nanostructures have been generated by chemical vapor deposition of a vanadium oxo-tri-isopropoxide precursor.<sup>46</sup> In a related technique, <30 nm VO<sub>2</sub> powders have even been obtained<sup>47</sup> through the pyrolysis of precursors such as [NH<sub>4</sub>]<sub>5</sub>[(VO)<sub>6</sub>(CO<sub>3</sub>)<sub>4</sub>(OH)<sub>9</sub>].10 H<sub>2</sub>O. Similarly, high-temperature annealing (1000 °C) in an argon atmosphere of VO<sub>2</sub> seed particles can induce the corresponding nucleation and growth of VO<sub>2</sub> nanorods.<sup>26</sup> By analogy, vapor deposition utilizing finely meshed VO<sub>2</sub> powder in the presence of He gas at a temperature range of 550 to 650 °C was recently used to synthesize high yields of single-crystalline VO<sub>2</sub> nanorods with a narrow width distribution.<sup>18</sup> Lastly, vapor transport methods have been used to generate crystalline, well-faceted VO<sub>2</sub> nanorods on a silicon nitride substrate at 900–1000 °C in the presence of bulk VO<sub>2</sub> and argon at a pressure of 12–13 Torr.<sup>48</sup>

Interestingly, vanadium sesquioxide (V<sub>2</sub>O<sub>3</sub>) also exhibits an interesting magnetic transition that accompanies the M–I transition. That is, at room temperature, vanadium sesquioxide acts as a paramagnetic metal. However, when it is cooled below its transition temperature, it converts into an anti-ferromagnetic insulator. Coincident with this transition, vanadium sesquioxide exhibits a structural transformation from rhombohedral symmetry at room temperature to a monoclinic structure below the transition temperature.<sup>49</sup> The interesting property changes associated with the M–I transition in vanadium sesquioxide render it a promising candidate for applications as diverse as temperature sensors, current regulators, and components of conductive polymer composites.<sup>50–53</sup>

Previous reports regarding the synthesis of nanoscale formulations of V<sub>2</sub>O<sub>3</sub> have involved a number of parallel tracks as well. For example, V<sub>2</sub>O<sub>3</sub> nanoparticles can be produced by means of laser-induced vapor-phase reaction. Moreover, spherical nanoparticles measuring 30 nm in diameter can be fabricated by reductive pyrolysis (to as high as 730 °C) of ammonium oxovanadium(IV) carbonate hydroxide in a H<sub>2</sub> flow.<sup>54</sup> In addition, stable and homogeneous V<sub>2</sub>O<sub>3</sub> nanocrystals can be grown<sup>9</sup> directly from the thermal reduction of V<sub>2</sub>O<sub>3</sub> thin films in vacuum at 600 °C as well as

through the thermal decomposition of oxalate.<sup>55</sup> V<sub>2</sub>O<sub>3</sub> and VN nanocrystals have been synthesized<sup>56</sup> by the decomposition of NH<sub>4</sub>VO<sub>3</sub> followed by nitridation in an autoclave with metallic Na flux at 450 to 600 °C. The reaction between transition metal alkoxides and benzyl alcohol<sup>57</sup> at temperatures of 200 to 220 °C has also provided a route towards the preparation of crystalline V<sub>2</sub>O<sub>3</sub> nanoparticles, measuring 20 to 50 nm. Furthermore, V<sub>2</sub>O<sub>3</sub> nanopowder can be successfully prepared through thermal decomposition of its corresponding oxalate.<sup>55</sup> Recently, hollow rutile VO<sub>2</sub> and corundum V<sub>2</sub>O<sub>3</sub> nanotubes have been generated through a H<sub>2</sub>-mediated reduction of V<sub>2</sub>O<sub>5–8</sub> nanoscroll precursors,<sup>58</sup> which themselves had been hydrothermally prepared from aged suspensions of V<sub>2</sub>O<sub>5</sub> and dodecylamine.<sup>58</sup>

In this paper, our approach to generating filled V<sub>2</sub>O<sub>3</sub> nanorods is inspired by this nanoscroll methodology, but with a VO<sub>2</sub>-based intermediate precursor template. Specifically, as a first step, we initially synthesized nanorods of hydrated VO<sub>2</sub> and dehydrated these samples by heating in an inert atmosphere at high temperature to yield VO<sub>2</sub> in a parallel fashion to what has already been reported for micron-scale powders.<sup>59</sup> It is worth reiterating that VO<sub>2</sub> possesses a high-temperature metallic state (VO<sub>2</sub>(R)) above 68 °C with a tetragonal rutile structure with parameters of  $a = b = 4.55 \text{ \AA}$  and  $c = 2.88 \text{ \AA}$ , in which each vanadium ion is located at the center of an oxygen octahedron.<sup>60–62</sup> The semiconducting low-temperature form, *i.e.* ambient room-temperature motif of VO<sub>2</sub>(M), is a monoclinic distortion of the rutile structure with  $a = 5.75 \text{ \AA}$ ,  $b = 4.52 \text{ \AA}$ , and  $c = 5.38 \text{ \AA}$ , involving a pairing and off-axis displacement of alternate vanadium ions along the rutile  $c$  axis.<sup>60,63,64</sup> Our second step was to essentially reduce VO<sub>2</sub> to V<sub>2</sub>O<sub>3</sub> in high yields at a high annealing temperature (*i.e.* over 550 °C) in a manner analogous to what has been accomplished with thin films.<sup>14</sup> Our methodology is also similar to the synthesis<sup>65</sup> of V<sub>2</sub>O<sub>3</sub> by the thermal decomposition of V<sub>2</sub>O<sub>5</sub> in high vacuum at 600 °C. While it may have been logical to have used a different variation of VO<sub>2</sub> intermediate in our syntheses, *i.e.* VO<sub>2</sub>(B), the metastable nature of this latter polymorph of VO<sub>2</sub> made it difficult to proceed with that particular route.<sup>10,66</sup>

Hence, the real novelty of this work lies in three key areas. First, we believe we are unique in achieving the production of filled, crystalline V<sub>2</sub>O<sub>3</sub> nanorods in reasonable quantities (*i.e.* as much as grams at a time in a given run). Second, our V<sub>2</sub>O<sub>3</sub> nanorods are relatively free of impurities as well as the presence of other phases of vanadium oxide, thereby removing the need for additional sample purification. In other words, we are not creating mixed valent VO<sub>*x*</sub> nanostructures, wherein species such as VO<sub>2</sub>, V<sub>2</sub>O<sub>5</sub>, and V<sub>6</sub>O<sub>13</sub> can potentially co-exist.<sup>38,41,67</sup> Third, we were able to generate these V<sub>2</sub>O<sub>3</sub> nanorods by building upon nanorod motifs of VO<sub>2</sub> itself as an intermediate stepping stone, a necessary precursor, to this product. We have previously demonstrated<sup>68</sup> the feasibility of this latter idea in our laboratory in our conversion of titanate nanorods and nanotubes into anatase TiO<sub>2</sub> nanorods and nanoparticles, respectively, at essentially 100% yield. In that case, we showed that the size and shape of the precursor titanate structural motif strongly dictated and controlled the eventual morphology of the resulting titania products.

## Experimental

### Synthesis

All chemicals were used as purchased, without further purification. The synthesis of hydrated VO<sub>2</sub> nanorods was conducted using a minor modification of a hydrothermal method previously presented by Gui *et al.*<sup>69</sup> We chose this particular protocol, because it avoided the high temperatures and specialized equipment associated with gas-phase techniques. Moreover, this procedure<sup>69</sup> could lead to the production of high-quality, single-crystalline nanorods in large quantities with reliable control over morphology without the need for sintering. Specifically, in a typical reaction, 0.2546 g of V<sub>2</sub>O<sub>5</sub> (Acros Organics, 99.6 + %) and 0.2412 g of KOH (Fisher Scientific) were added to a 23 mL Teflon lined autoclave. Subsequently, 14.38 mL of H<sub>2</sub>O was added to the autoclave and the solution was mixed thoroughly, achieving final molar concentrations of 0.10 and 0.29 M for V<sub>2</sub>O<sub>5</sub> and KOH, respectively. Following this process, 50.7 μL of hydrazine (Acros Organics, 99%), selected not only for its reducing ability but also for its potential in coordinating central vanadium ions into a one-dimensional morphology,<sup>69</sup> was added to the tune of 0.068 M, followed by further mixing of the solution. Finally, the pH of the solution was adjusted to ~3 using HCl (EMD, ACS reagent grade). The autoclave was subsequently sealed and heated at 150 °C for 48 h. After heating, a blue-black product was isolated and purified by centrifugation and washing with absolute ethanol (Acros Organics, 200 proof) followed by storage in an inert atmosphere to prevent additional oxidation.

To prepare the dehydrated form of VO<sub>2</sub>, the product of the hydrothermal reaction was heated under N<sub>2</sub> at 350 °C for 24 h which, at elevated temperatures, likely directly generated the thermodynamically most stable VO<sub>2</sub>(R) form, which subsequently reversibly converted to VO<sub>2</sub>(M) at room temperature under ambient conditions. To synthesize V<sub>2</sub>O<sub>3</sub>, the blue-black VO<sub>2</sub> product in either its hydrated or dehydrated formulation was heated at 800 °C at a ramp rate of 10 °C min<sup>-1</sup>. The black sample was subsequently removed from the oven and allowed to cool to room temperature under a reducing atmosphere so as to prevent oxidation of the product.

### Characterization

The diameters and lengths of as-prepared nanorods were initially characterized using a field emission scanning electron microscopy instrument (FE-SEM Leo 1550), operating at an accelerating voltage of 15 kV and equipped with energy-dispersive X-ray spectroscopy (EDS) capabilities, as well as with a Hitachi S-4800 at an accelerating voltage of 1.0 kV. Samples for SEM were prepared by dispersing as-prepared nanorods in ethanol, sonicating for about 2 min and then depositing the sample onto a silicon wafer, attached to a SEM aluminum stub.

Low magnification TEM images were taken at an accelerating voltage of 80 kV on a FEI Tecnai12 BioTwinG<sup>2</sup> instrument, equipped with an AMT XR-60 CCD Digital Camera System. High-resolution TEM (HRTEM) images were obtained on a

JEOL 2010F instrument at accelerating voltages of 200 kV. Specimens for all of these TEM experiments were prepared by dispersing the as-prepared product in ethanol, sonicating for 2 min to ensure adequate dispersion of the nanorods, and depositing one drop of the solution onto a 300 mesh Cu grid, coated with a lacey carbon film.

To prepare powder X-ray diffraction (XRD) samples, the resulting nanorods were rendered into slurries in ethanol, sonicated for about 1 min, and then air-dried upon deposition onto glass slides. Diffraction patterns were collected using a Scintag diffractometer, operating in the Bragg-Bretano geometry and using Cu Kα radiation ( $\lambda = 1.54 \text{ \AA}$ ) from  $10 \leq 2\theta \leq 80^\circ$  at a scanning rate of 2° in 2θ per minute. Temperature-resolved synchrotron XRD data were collected at the X7B beamline at the National Synchrotron Light Source. Sample powders were loaded in a polyimide capillary with a 0.5 mm inner diameter. The X-ray beam size was adjusted using slits to match the capillary size. Temperature was controlled by an air-blow type heater with the thermocouple placed in contact with the outside of the capillary in the middle of the air stream from the heater. A 2 °C/step temperature scan started from 55 °C for the heating cycle, with at least 30 min stay at each step. The subsequent cooling started from 69 °C with the same temperature step size. 2-D XRD data were collected using a MAR345 imaging plate area detector with continuous 120 s exposure times. The readout time for the detector was 45 s between exposures. 2-D data were processed by the program Fit2D to obtain traditional 1-D “2θ scan” data for analysis. The wavelength used was 0.31840(2) Å.

### Measurements

Magnetic measurements were performed on a 11.46 mg powder sample of V<sub>2</sub>O<sub>3</sub> nanowires in a Quantum Design Magnetic Property Measurement System (MPMS) with fields up to 7 T and temperatures between 1.8 and 300 K.

Nanorod devices were fabricated by a combination of electron beam (e-beam) lithography and e-beam induced direct metal deposition (EBID) using a scanning electron microscope (SEM) (Helios, FEI) equipped with a Nano Pattern Generating System (NPGS) and an organometallic gas injection system (GIS). First, contact pads measuring 100 × 100 μm<sup>2</sup> in area and electrodes with 1 μm in width and spacing were fabricated using e-beam lithography on a Si substrate with 400-nm thick thermally grown SiO<sub>2</sub>. In a typical run, a layer of the commercial e-beam resist, ZEP-1, was applied *via* spin-coating onto the substrate at 3000 rpm followed by 3 min of baking at 180 °C. The substrate was subsequently loaded into the SEM. Contact pads and electrode patterns were then exposed by e-beam irradiation (at 30 kV accelerating voltage and 1.4 nA current), followed by development in xylenes for 2 min and rinsing in isopropyl alcohol. Finally, 40-nm thick platinum was deposited onto the substrate surface by sputter coating in a vacuum atmosphere of ~10<sup>-5</sup> Torr.

V<sub>2</sub>O<sub>3</sub> nanorods were then randomly transferred onto the substrate containing the fabricated contact pads by spin-coating a suspension of these nanomaterials dispersed in aqueous solution at 1000 rpm. Upon location of these V<sub>2</sub>O<sub>3</sub> nanorods

on the substrate using the SEM, platinum electrical contacts, maintaining a thickness of  $\sim 100$  nm and a width of  $\sim 80$  nm, were applied to the nanorods by direct deposition of Pt itself, derived from decomposition of a trimethyl [(1,2,3,4,5-ETA)-1-methyl-2,4-cyclopentadien-1-yl] platinum source, that had been introduced into the vacuum chamber by a GIS, in the presence of a 30 kV e-beam with a 1.4 nA current. Current–voltage ( $I$ – $V$ ) measurements were obtained using a HFTTP4 cryogenic probe station (Lakeshore) spanning a temperature ( $T$ ) range from 80 K to 300 K.

## Results and discussion

### 1 Structural characterization and mechanism

As can be seen from the XRD patterns shown in Fig. 1, the samples synthesized are pure with no peaks attributable to crystallographic impurities within the detection limits of the instrument. Specifically, as expected, the dehydrated VO<sub>2</sub> XRD pattern can be indexed to a monoclinic structure (JCPDS #82-0661) with space group  $P2_1/c$ . Lattice parameters of  $a = 5.750 \pm 0.008$  Å,  $b = 4.523 \pm 0.007$  Å, and  $c = 5.376 \pm 0.018$  Å were calculated based on the powder XRD pattern, and are in excellent agreement with those reported in the JCPDS database, namely  $a = 5.752$  Å,  $b = 4.526$  Å, and  $c = 5.383$  Å. We actually collected an XRD pattern of a dried powder sample of hydrated VO<sub>2</sub> itself in Fig. S1 for the sake of completeness.† The quality of that data, however, may be partially attributable to the

incompatibility between the ‘hydrated’ nature of the sample and the ‘dry’ sample acquisition process itself, as well as to the presence of impurities that were subsequently transformed during later high-temperature annealing treatments.

The XRD pattern for V<sub>2</sub>O<sub>3</sub> can be indexed on the basis of a rhombohedral unit cell (JCPDS #85-1411) space group,  $R\bar{3}c$ . Lattice parameters determined in the hexagonal setting from the experimental powder XRD pattern indicate that  $a = 4.954 \pm 0.010$  Å and  $c = 13.939 \pm 0.045$  Å, in good agreement with the corresponding literature values of  $a = 4.952$  Å and  $c = 14.003$  Å.

Electron microscopy on the as-prepared sample, Fig. 2a and b, showed that the VO<sub>2</sub>·H<sub>2</sub>O nanorods possess widths of  $74 \pm 21$  nm and lengths of up to several microns. The HRTEM image in Fig. 2b, in particular, shows lattice spacings, measuring 0.485 nm and 0.515 nm, respectively, which are in good agreement with the expected (JCPDS #13-0346) literature values of 0.434 nm and 0.512 nm, respectively. The sharpness of the spots in the selected area electron diffraction, SAED, pattern shown in Fig. 2c, strongly suggests that the nanorods are highly crystalline. However, measured

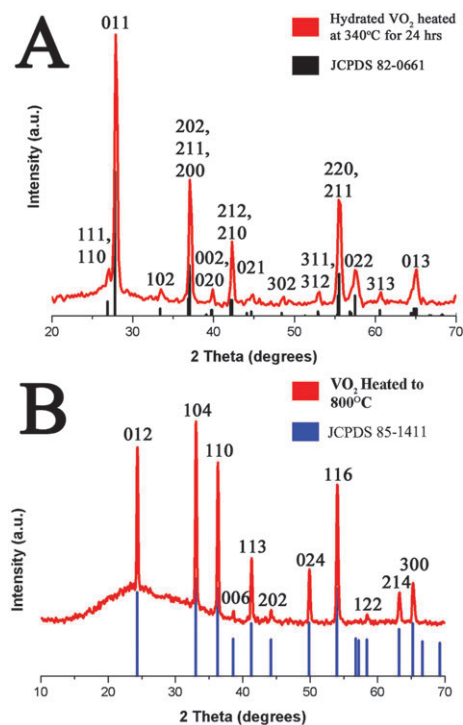


**Fig. 1** (A). XRD patterns corresponding to as-obtained, dehydrated samples and the associated JCPDS #82-0661 for VO<sub>2</sub>(M). (B) XRD pattern of V<sub>2</sub>O<sub>3</sub> obtained by heating of a VO<sub>2</sub> precursor in a hydrogen atmosphere to 800 °C, along with the corresponding database standard, JCPDS #85-1411.

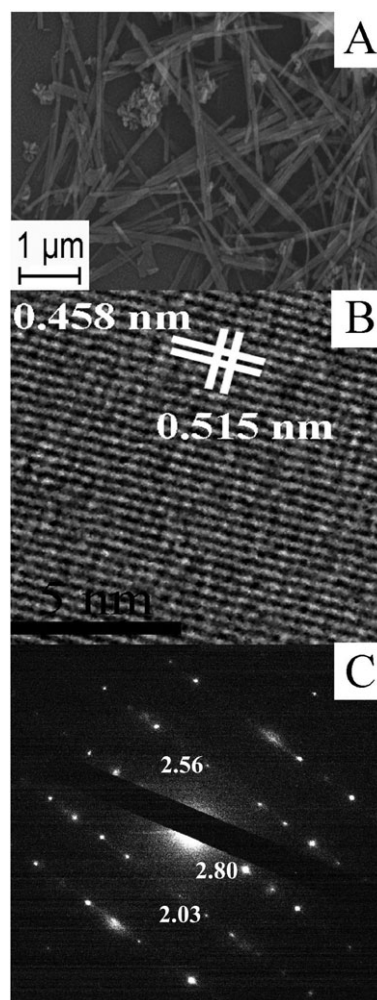


**Fig. 2** (A) SEM image of as-prepared VO<sub>2</sub>·H<sub>2</sub>O nanorods. (B) HRTEM image of a typical, individual hydrated nanorod. (C) SAED of the nanorod probed in (B). Measured  $d$ -spacings in Angstroms are indicated directly to the left of indexed diffraction spots.

$d$ -spacings from the SAED pattern and its XRD pattern (Fig. S1†) did not match well with one another, an observation which can be reasonably attributed to sample dehydration (and corresponding lattice alteration) under electron beam irradiation, characteristic of TEM sampling conditions. Hence, we were unable to properly index the diffraction pattern.

To probe the expected structural alteration associated with the M–I transition of VO<sub>2</sub>(M) to VO<sub>2</sub>(R), our as-prepared nanostructures were heated in an inert atmosphere to 350 °C for 4 h in order to facilitate dehydration.<sup>69</sup> The SEM image in Fig. 3a shows that the resulting morphology of the wires remained mostly one-dimensional, with some shrinkage due to the loss of water. That is, the dehydration process did not appear to damage the regular arrangement of V and O atoms.<sup>69</sup> We measured an average width of  $68 \pm 12$  nm with lengths of up to several microns for our structures. HRTEM and SAED data presented in Fig. 3b and c on our VO<sub>2</sub> nanorods further confirm that they remain single crystalline after dehydration. In particular, the HRTEM data clearly show lattice planes with a  $d$ -spacing of 0.323 nm, corresponding to the (110) plane ( $d = 0.331$  nm) of monoclinic VO<sub>2</sub>, while the SAED pattern shows the presence of intense spots, corresponding to the (110), (212), and (102) planes, in good agreement not only with our HRTEM data but also with our diffraction data.

As was previously described in Fig. 1, we obtained evidence for the formation of monoclinic VO<sub>2</sub> upon dehydration of

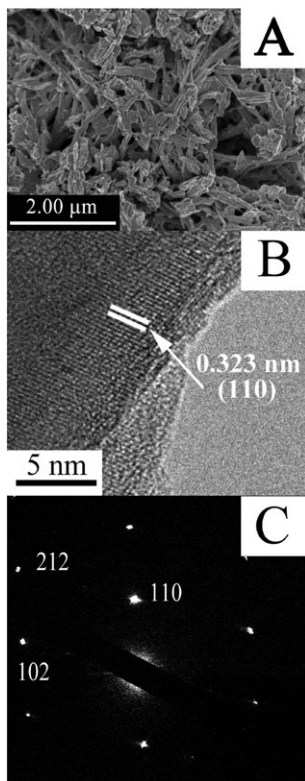


**Fig. 3** (A) SEM image of dehydrated VO<sub>2</sub> nanorod aggregates with individual widths of  $68 \pm 12$  nm and lengths of up to a couple of microns. (B) HRTEM image of a single VO<sub>2</sub> nanorod. (C) SAED of the VO<sub>2</sub> nanorod probed in (B).

VO<sub>2</sub>·H<sub>2</sub>O. To further investigate the quality of our sample, we sought to investigate the transition from the VO<sub>2</sub>(M) to the VO<sub>2</sub>(R) phase, using temperature-dependent *in situ* synchrotron radiation measurements. What we found, as shown in Fig. 4, was that the transition temperature spanned 63–65 °C during the heating cycle and 61–59 °C during the subsequent cooling cycle. This rather small hysteresis is consistent with an expected rapid and reversible transformation,<sup>70</sup> as the positions and intensities of the peaks returned to their original profiles upon cooling.

The Mott transition is brought on by a change in crystalline structure presumably due to changes in the dimensions of the unit cell.<sup>18</sup> Observed peak shifts likely represent the shrinkage of the unit cell, as expected with the conversion from the monoclinic to the rutile form. Upon confirmation of the validity of this transition at the nanoscale, we then set about converting our 1D nanorod sample from the starting formulation of VO<sub>2</sub> to the final V<sub>2</sub>O<sub>3</sub> chemical structure. As previously mentioned, there have been a number of reports in the literature pertaining to the conversion of VO<sub>2</sub> to V<sub>2</sub>O<sub>3</sub>.<sup>14,65</sup> Herein, we heated our sample, consisting of either VO<sub>2</sub>·H<sub>2</sub>O or VO<sub>2</sub> in H<sub>2</sub> at temperatures ranging from 500–900 °C and using reaction times up to 5 h so as to obtain V<sub>2</sub>O<sub>3</sub> nanorods. Experimentally, we found that heating of the sample to 800 °C using a ramp rate of 10 °C min<sup>-1</sup> followed by subsequent cooling to room temperature yielded the best results, as defined by the resulting sample purity and crystallinity as well as the prevailing nanorod morphology.

SEM and TEM data on this optimized sample are shown in Fig. 5. Though nanorods predominate, samples are not necessarily monodisperse, with the presence of nanorods to nanoparticles in the ratio of 3 : 1. Nonetheless, the widths and lengths of the as-prepared V<sub>2</sub>O<sub>3</sub> nanorods are slightly smaller than those of the precursor VO<sub>2</sub> nanorods, measuring  $64 \pm 18$  nm in diameter and up to a couple of microns in length, respectively. The morphology of the as-prepared wires also changed slightly as well, transforming from relatively smooth wires to wires with a roughened surface texture, perhaps due to the presence of V<sub>2</sub>O<sub>3</sub> particulates. HRTEM images, shown in Fig. 5a and b, show that the wires remain highly crystalline, with clearly visible lattice planes possessing measured  $d$ -spacings of 0.248 nm and 0.268 nm, that correlate with the (110) ( $d = 0.247$  nm) and (104) ( $d = 0.271$  nm) planes of V<sub>2</sub>O<sub>3</sub>, respectively, as supported by literature data (JCPDS #85-1411). These experimental values are also in good agreement with data taken from powder XRD measurements, Fig. 1a, where the calculated  $d$ -spacings of 0.248 nm and 0.271 nm can be assigned to the (110) and (104) peaks, respectively.

Previous reports have also shown that conversion of films and nanocrystals of VO<sub>2</sub> to V<sub>2</sub>O<sub>3</sub> can be explained *via* a combination of diffusion, coalescence, and stabilization processes,<sup>9,65</sup> which is consistent with what we have observed here. Of relevance here, it was noted that the thermal reduction process involved in one of those experiments<sup>9</sup> involved rearrangement of oxygen polyhedra surrounding the V atoms; the reduced oxide phases essentially diffused and coalesced, leading to the formation of differently-shaped geometries. Hence, the thermally-induced (a) nucleation and growth of

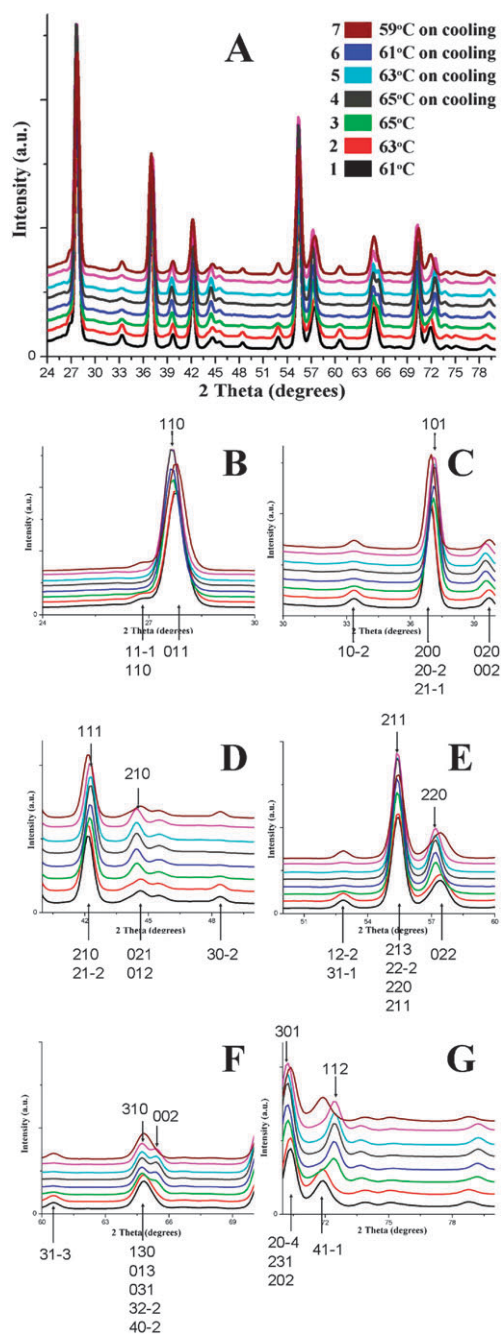


**Fig. 4** (A) Variable-temperature synchrotron diffraction data re-plotted over  $24^\circ \leq 2\theta \leq 80^\circ$  to simulate the familiar scale for Cu  $K\alpha$  radiation ( $\lambda = 1.5418 \text{ \AA}$ ) commonly used on laboratory sources. The original data were collected using  $\lambda = 0.3184 \text{ \AA}$  on a synchrotron source. Indexing of peaks (monoclinic  $P2_1/c$  bottom and tetragonal  $P4_2/mmm$  top) for individual sections of the diffraction pattern are shown in (B)  $24^\circ \leq 2\theta \leq 30^\circ$ , (C)  $30^\circ \leq 2\theta \leq 40^\circ$ , (D)  $40^\circ \leq 2\theta \leq 50^\circ$ , (E)  $50^\circ \leq 2\theta \leq 60^\circ$ , (F)  $60^\circ \leq 2\theta \leq 70^\circ$ , and (G)  $70^\circ \leq 2\theta \leq 80^\circ$ . Disappearance of certain peaks are a diagnostic for the transition from the monoclinic to the tetragonal phase in  $\text{VO}_2$ : for example, the disappearance of monoclinic peaks (11-1,110) in (B), 30-2 in (D), (12-2, 31-1) in (E), and the 31-3 in (F).

the  $\text{V}_2\text{O}_3$  phase, governed to a large extent by atomic diffusion, and (b) the formation of lattice defects during the *in situ* phase transformation along microstructural defects of the parent

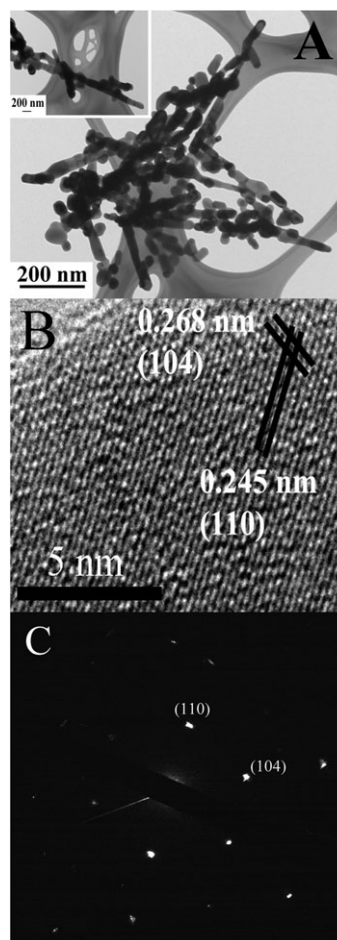


**Fig. 5** (A) TEM image of  $\text{V}_2\text{O}_3$  nanorods. Inset shows a different region containing these metal oxide nanorods. (B) HRTEM image of a representative, individual nanorod, showing lattice spacings consistent with the (104) and (110) planes of  $\text{V}_2\text{O}_3$ . (C) SAED pattern of  $\text{V}_2\text{O}_3$  nanorods, demonstrating their single crystallinity.

precursor  $\text{VO}_2$  likely yielded a highly strained intermediate defective state.<sup>65</sup> Diffusion is expected to occur isotropically, so that the transformed phase could initially have formed spherical particles. These particles then presumably coalesced to generate roughened, high-surface-energy nanorod-like motifs. Yet, these as-prepared  $\text{V}_2\text{O}_3$  nanomaterials could also exist stably as spheres, since defect density was minimized and the presence of high surface energy surfaces was reduced in this particular geometric configuration.

We indeed noted that as the reaction time and temperature were increased, fewer nanorods were produced but a preponderance of nanoparticles was clearly noted in the sample. Moreover, consistent with this growth mechanism, we also discovered that temperature was the main parameter governing this reaction. That is, our reaction medium needed to be ‘hot’ enough, *i.e.* heated above  $800^\circ\text{C}$ , in order for the conversion from  $\text{VO}_2$  to  $\text{V}_2\text{O}_3$  to occur. At temperatures below  $800^\circ\text{C}$ , the morphology of the sample retained its nanorod motif, but the product actually consisted of a mixture of different phases (including  $\text{V}_6\text{O}_{13}$  and  $\text{V}_3\text{O}_7$ ) of vanadium oxide. Hence, our observations could be explained by *in situ* phase conversions, as evinced by diffraction analyses.

## 2 Measurements

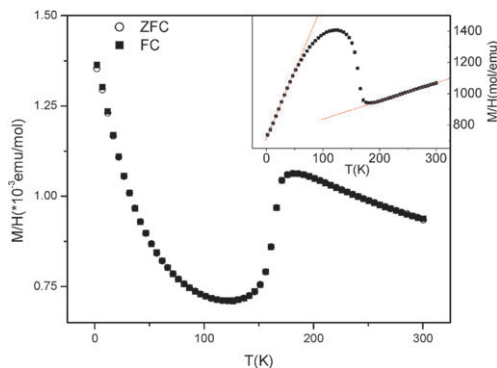
**A Magnetic data.** The temperature variation of the magnetic susceptibility  $M/H$  ( $H = 5.0$  T) for  $V_2O_3$  is plotted in Fig. 6, for both ZFC (zero field cooled) as well as FC (field cooled at 5.0 T) cases. The magnetic susceptibility ( $M/H$ ) was found to slowly increase from 300 K to about 200 K, with an anomalous drop in magnetic susceptibility observed at about 166 K. The magnetic susceptibility subsequently increased again at lower temperatures. We can fit the magnetic susceptibility data above 200 K using the Curie–Weiss law in eqn (1):

$$M/H = C/(T - \theta_p) \quad (1)$$

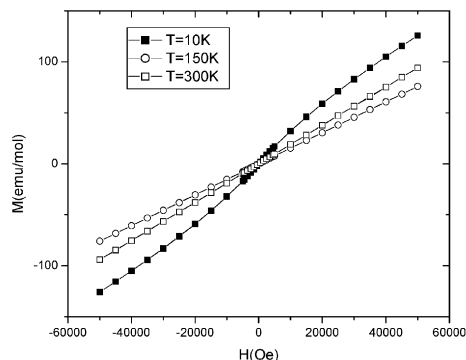
The Curie constant,  $C$  ( $C = N\mu_{\text{eff}}^2/3k_B$  where  $N$  is the number of V atoms per unit cell), yields an effective paramagnetic moment per V atom,  $\mu_{\text{eff}} = 2.64 \mu_B$ , which is close to the Hund's rule value for  $V^{3+}$ , namely  $\mu_{\text{eff}} = 2.8 \mu_B$ . The calculated paramagnetic Curie temperature,  $\theta_p$ , is about  $-634$  K. The negative value here also indicates that the V moments are antiferromagnetically coupled. Both  $C$  and  $\theta_p$  are in good agreement with the reported behavior for bulk  $V_2O_3$ .<sup>71</sup>

Fig. 7 represents the measurement of the field dependence of the magnetization from  $-5.0$  T to  $5.0$  T at different temperatures. At high temperatures,  $M$  is linear with the field. Fig. 6 and 7 suggest that the V moments are spatially localized and fluctuate independently above the 166 K anomaly. The anomaly observed here agrees well with that of pure bulk  $V_2O_3$ , where it corresponds to the simultaneous onset of antiferromagnetic order and the delocalization of the V  $d$ -electrons. Also since the oxygen stoichiometry can significantly change the phase transition behavior,<sup>71</sup> the anomaly at 166 K may indicate that our nanorod sample is very close to the expected stoichiometric ratio of  $V_2O_3$  without the presence of impurities or extraneous vanadium oxide phases.

A second region of Curie–Weiss behavior has been observed at the lowest temperatures. That is, Fig. 7 shows a weak nonlinearity in  $M$  vs.  $H$  behavior at 10 K, as expected for the paramagnetic Brillouin function. Here, the fitted Curie–Weiss law results in a significantly smaller Curie



**Fig. 6** Temperature dependence of the DC magnetization at  $H = 5.0$  T. Both ZFC and FC curves at 5.0 T were measured, although little hysteresis was observed. Inset:  $H/M$  vs.  $T$ , showing that the linear regions, above 200 K and below 50 K, can be fit well with the Curie–Weiss law, where the slope gives the inverse of the Curie constant ( $1/C$ ).



**Fig. 7** DC magnetization measured at three different temperatures (*i.e.* 10 K, 150 K, and 300 K) with fields from  $-50\,000$  Oe to  $50\,000$  Oe.

**Table 1** Curie–Weiss fit parameters ( $M/H = C/(T - \theta_p)$ ) with ( $C = N\mu_{\text{eff}}^2/3k_B$ ) from  $M$  vs.  $T$  measurements

$T/K$	$C/\text{emu K mol}^{-1}$	$\theta_p/K$	$\mu_{\text{eff}}/\mu_B$
$> 200$	0.874	$-633.9$	2.64
$< 50$	0.115	$-82.5$	0.96

constant than the one found above 166 K (Table 1), implying that only a subset of the V atoms remains paramagnetic at low temperature. Yet, the moment concentration is sufficiently high that this second Curie–Weiss contribution to the susceptibility cannot originate with moment-bearing impurities and hence, must be intrinsic. Previous researchers<sup>72,73</sup> have suggested that the surface spins in antiferromagnetic nanoparticles are uncompensated, and may produce a paramagnetic susceptibility below the overall Néel temperature, just as we have found with our  $V_2O_3$  nanorods herein.

We suggest that the magnetization data shown in Fig. 6 and 7 represent the sum of the contributions both from the surface and the core spins. Above the 166 K transition temperature where antiferromagnetic order sets in, all V moments are paramagnetic, just as in the bulk material. By contrast, below the transition temperature, the interior of the nanoparticle is antiferromagnetic, while the spins on the surface are either free or paramagnetic. When the temperature is low enough, these surface spin contributions dominate, and this situation leads to the observed increase in susceptibility at low temperatures.

**B Electronic-transport characterization.** A typical device consisted of a  $\sim 1 \mu\text{m}$  long  $V_2O_3$  wire section (SEM image in Fig. 8, labeled C) electrically contacted on opposite ends by large-scale lithographically-defined pads (Fig. 8, labeled A) and smaller scale EBID-defined platinum leads (Fig. 8, labeled B). The device two-terminal current–voltage ( $I$ – $V$ ) characteristic was symmetric with respect to the sign of voltage bias for all measured temperatures (*e.g.* three representative temperatures are shown in Fig. 9), indicating similar electrical contact properties between the EBID-platinum wire and the  $V_2O_3$  nanorod on both ends of the device.

The measured device current increased linearly with voltage over the bias range of  $0.3 \text{ V} < |V| < 5 \text{ V}$  for every measured temperature (80–300 K) (Fig. 9). We calculated the two-probe  $V_2O_3$  nanorod resistivity ( $\rho$ ) from the device's ohmic resistance ( $R \equiv V/I$ ) according to  $\rho \equiv R \cdot A/L$ , where  $A$  is the cross-sectional

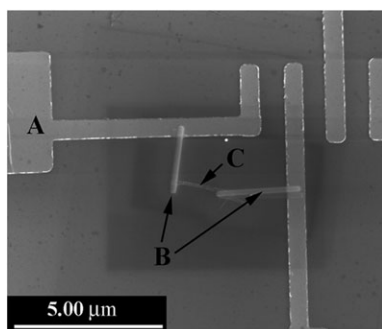


**Fig. 8** SEM image of a  $V_2O_3$  nanorod device used for electronic measurements. (A) Electrodes deposited by a Lesker sputter coater. (B) Electrodes deposited by the EBID technique. (C) A representative  $V_2O_3$  nanorod.

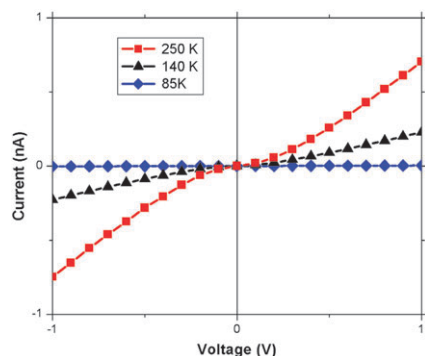


**Fig. 9**  $I$ - $V$  curves taken on a  $V_2O_3$  nanorod at three different temperatures, associated with the warming cycle, at 250 K (red squares), 140 K (black triangles), and 85 K (blue diamonds).

nanorod area and  $L$  is the length of the nanorod bounded by the two Pt contacts. We assumed a circular nanorod cross-sectional area,  $A = \pi r^2$ , with  $r$  as the nanorod radius measured from SEM images. At low applied voltage bias ( $-0.3 < V < 0.3$  V), the  $I$ - $V$  curve was slightly nonlinear, likely indicating a small Schottky barrier at the Pt- $V_2O_3$  contact (Fig. 9).

Nanorod device two-terminal resistivity ( $\rho$ ) increased with decreasing temperature (Fig. 10), with a total resistivity change ( $\Delta\rho$ ) of  $\sim 10^3$  upon changing the temperature from 300 K to 80 K. Despite the two-terminal nature of our measurements, separate measurements of minimal changes in the Pt lead resistance over the same temperature range (not shown) allowed us to ascribe the observed behavior to the  $V_2O_3$  nanorod itself. Upon cooling the device, we observed an increase in the rate of nanorod resistivity change in the temperature range around 150–200 K (red open triangles), similar to the point at which we observed large changes in nanorod magnetization (Fig. 6), and consistent with previous reports of a metal-insulator transition<sup>74</sup> in  $V_2O_3$  at temperatures of around  $\sim 150$  K. The total magnitude of resistivity change has previously been used to infer information about material purity in terms of stoichiometry and crystallinity.<sup>14</sup> The nanorod device resistivity decreased smoothly over the entire temperature range upon warming from 80–300 K (Fig. 10, black solid squares), such that the entire temperature cycle is hysteretic, consistent with previously reported measurements<sup>74</sup> of corundum  $V_2O_3$  nanotubes.<sup>58</sup> Moreover,

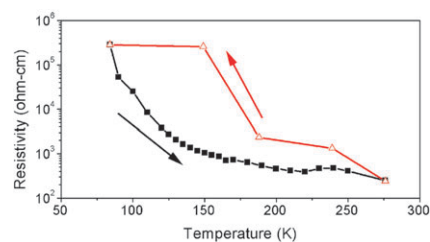


**Fig. 10** Plot of resistivity vs. temperature during the cooling cycle (red, open triangles) and the warming cycle (black, solid squares) for  $V_2O_3$  nanorods.

previous observations of similar hysteresis in  $V_2O_3$  film resistivities have been discussed in terms of substrate-induced volume confinement effects.<sup>75</sup>

## Conclusions

$VO_2$  nanorods have been initially generated as reactive precursors. Structural changes, associated with the M-I transition, from the monoclinic form to the rutile form have been investigated and confirmed using XRD and synchrotron data, showing that the structural transition is reversible and occurs at around 63 °C. When this sample was subsequently heated to 800 °C in a reducing atmosphere, it was successfully converted to  $V_2O_3$  with effective retention of its one-dimensional morphology. Furthermore, we have collected both magnetic and transport data on our samples, which are in general agreement with either bulk behavior or prior results on analogous nanoscale systems.

## Acknowledgements

Research carried out (in whole or in part) at the Center for Functional Nanomaterials at Brookhaven National Laboratory was supported by the US Department of Energy, Office of Basic Energy Sciences, under Contract No. DE-AC02-98CH10886. MCA and SSW specifically acknowledge the US Department of Energy (DE-AC02-98CH10886) for facility and personnel support for work completed in the Condensed Matter Physics and Materials Science Department. JBP thanks the National Science Foundation (DMR-0800415) for overall support. SSW also acknowledges the National Science Foundation (CAREER Award DMR-0348239), and the Alfred P. Sloan Foundation for PI support and experimental supplies. Moreover, we are grateful to D. Wang (Boston College) as well as to H. Zhou and S. van Horn (SUNY Stony Brook) for their assistance with electron microscopy. We thank Dr Fernando Camino for helpful comments and assistance with our transport measurements.

## References

- 1 R. Muanghlua, N. Vittayakorn and A. Ruangphanit, *Aust. J. Basic Appl. Sci.*, 2008, **2**, 406.
- 2 M. Law, L. E. Greene, J. C. Johnson, R. Saykally and P. Yang, *Nat. Mater.*, 2005, **4**, 455.
- 3 P. Wang, S. M. Zakeeruddin, J. E. Moser, M. K. Nazeeruddin, T. Sekiguchi and M. Gratzel, *Nat. Mater.*, 2003, **2**, 402.
- 4 J. Tang, J. R. Durrant and D. R. Klug, *J. Am. Chem. Soc.*, 2008, **130**, 13885.

- 5 A. Kleiman-Shwarscstein, Y. S. Hu, A. J. Forman, G. D. Stucky and E. W. McFarland, *J. Phys. Chem. C*, 2008, **112**, 15900.
- 6 V. Galvita, T. Hempel, H. Lorenz, L. K. Rihko-Struckmann and K. Sundmacher, *Ind. Eng. Chem. Res.*, 2008, **47**, 303.
- 7 J. A. Rodriguez, S. Ma, P. Liu, J. Hrbek, J. Evans and M. Perez, *Science*, 2007, **318**, 1757.
- 8 N. Lopez, J. Gomez-Segura, R. P. Marin and J. Perez-Ramirez, *J. Catal.*, 2008, **255**, 29.
- 9 C. V. Ramana, S. Utsunomiya, R. C. Ewing and U. Becker, *Solid State Commun.*, 2006, **137**, 645.
- 10 W. Chen, J. Peng, L. Mai, H. Yu and Y. Qi, *Chem. Lett.*, 2004, **33**, 1366.
- 11 N. Ballardini, A. Battisti, F. Cavani, A. Cericola, C. Cortelli, M. Ferrari, F. Trifiro and P. Arpentini, *Appl. Catal. A*, 2006, **307**, 148.
- 12 E. V. Kondratenko, O. Ovsitser, J. Radnik, M. Schneider, R. Kraehnert and U. Dingerdissen, *Appl. Catal. A*, 2007, **319**, 98.
- 13 F. J. Morin, *Phys. Rev. Lett.*, 1959, **3**, 34.
- 14 S. J. Yun, B. G. Chae, J. W. Lim, J. S. Noh and H. T. Kim, *Electrochem. Solid-State Lett.*, 2008, **11**, 173.
- 15 C. F. Tsang, J. Kim and A. Manthiram, *J. Mater. Chem.*, 1998, **8**, 425.
- 16 C. Tsang and A. Manthiram, *J. Electrochem. Soc.*, 1997, **144**, 520.
- 17 D. S. Toledano, P. Metcalf and V. Henrich, *Surf. Sci.*, 2000, **449**, 19.
- 18 J. M. Baik, M. H. Kim, C. Larson, A. M. Wodtke and M. Moskovits, *J. Phys. Chem. C*, 2008, **112**, 13328.
- 19 G. A. Rozgonyi and W. J. Polito, *J. Electrochem. Soc.*, 1968, **115**, 56.
- 20 J. Shi, S. Zhou, B. You and L. Wu, *Solar Energy Mater. Solar Cells*, 2007, **91**, 1856.
- 21 B. G. Chae, H. T. Kim, S. J. Yun, B. J. Kim, Y. W. Lee, D. H. Youn and K. Y. Kang, *Electrochem. Solid-State Lett.*, 2006, **9**, C12.
- 22 L. Q. Mai, W. Chen, Q. Xu, J. F. Peng and Q. Y. Zhu, *Chem. Phys. Lett.*, 2003, **382**, 307.
- 23 C. Tenaillon, E. Suard, J. Rodriguez-Carvajal and P. Lacorre, *J. Magn. Magn. Mater.*, 2004, **278**, 57.
- 24 D. S. Toledano, P. Metcalf and V. E. Henrich, *Surf. Sci.*, 2001, **472**, 21.
- 25 J. B. Goodenough, *J. Solid State Chem.*, 1971, **3**, 490.
- 26 R. Lopez, T. E. Haynes, L. A. Boatner, L. C. Feldman and R. F. Haglund Jr, *Opt. Lett.*, 2002, **27**, 1327.
- 27 A. Cavalleri, C. Toth, C. W. Siders, J. A. Squier, F. Raksi, P. Forget and J. C. Kieffer, *Phys. Rev. Lett.*, 2001, **87**, 237401.
- 28 Y. Muraoka and Z. Hiroi, *Appl. Phys. Lett.*, 2002, **80**, 583.
- 29 R. A. Aliev and V. A. Klimov, *Phys. Solid State*, 2004, **46**, 532.
- 30 I. Balberg and S. Trokman, *J. Appl. Phys.*, 1975, **46**, 2111.
- 31 C. Lampe-Oennerud, J. O. Thomas, M. Hardgrave and S. Yde-Andersen, *J. Electrochem. Soc.*, 1995, **142**, 3648.
- 32 P. Liu, S. H. Lee, H. M. Cheong, C. E. Tracy, J. R. Pitts and R. D. Smith, *J. Electrochem. Soc.*, 2002, **149**, H76.
- 33 G. Sudant, E. Baudrin, B. Dunn and J. M. Tarascon, *J. Electrochem. Soc.*, 2004, **151**, A666.
- 34 A. Azens, G. Gustavsson, R. Karmhag and C. G. Granqvist, *Solid State Ionics*, 2003, **165**, 1.
- 35 F. Chudnovski, S. Luryi and B. Spivak, in *Future trends in microelectronics: the nano millenium*, ed. A. Zaslavsky, Wiley-Interscience, 2002, pp. 148.
- 36 X. Chen, X. Wang, Z. Wang, J. Wan, J. Liu and Y. Qian, *Nanotechnology*, 2004, **15**, 1685.
- 37 W. Chen, L. Mai, Y. Qi and Y. Dai, *J. Phys. Chem. Solids*, 2006, **67**, 896.
- 38 A. Liu, M. Ichihara, I. Honma and H. Zhou, *Electrochem. Commun.*, 2007, **9**, 1766.
- 39 M. Niederberger, H.-J. Muhr, F. Krumeich, F. Bieri, D. Gunther and R. Nesper, *Chem. Mater.*, 2000, **12**, 1995.
- 40 J. M. Reinoso, H.-J. Muhr, F. Krumeich, F. Bieri and R. Nesper, *Helv. Chim. Acta*, 2000, **83**, 1724.
- 41 H.-J. Muhr, F. Krumeich, U. P. Schonholzer, F. Bieri, M. Niederberger, L. J. Gauckler and R. Nesper, *Adv. Mater.*, 2000, **12**, 231.
- 42 F. Krumeich, H.-J. Muhr, M. Niederberger, F. Bieri and R. Nesper, *Z. Anorg. Allg. Chem.*, 2000, **626**, 2208.
- 43 F. Krumeich, H.-J. Muhr, M. Niederberger, F. Bieri, B. Schnyder and R. Nesper, *J. Am. Chem. Soc.*, 1999, **121**, 8324.
- 44 M. E. Spahr, P. Stoschitzki-Bitterli, R. Nesper, O. Haas and P. Novak, *J. Electrochem. Soc.*, 1999, **146**, 2780.
- 45 S. Choi, B.-J. Kim, Y. W. Lee, S. J. Yun and H.-T. Kim, *Jpn. J. Appl. Phys.*, 2008, **47**, 3296.
- 46 S. Mathur, T. Ruegamer and I. Grobelsek, *Chem. Vap. Deposition*, 2007, **13**, 42.
- 47 C. Zheng, X. Zhang, J. Zhang and K. Liao, *J. Solid State Chem.*, 2001, **156**, 274.
- 48 B. S. Guiton, Q. Gu, A. L. Prieto, M. S. Gudixsen and H. Park, *J. Am. Chem. Soc.*, 2005, **127**, 498.
- 49 B. S. Allimi, S. P. Alpay, C. K. Xie, B. O. Wells, J. I. Budnick and D. M. Pease, *Appl. Phys. Lett.*, 2008, **92**, 202105.
- 50 F. Sediri and N. Gharbi, *Mater. Sci. Eng.*, 2005, **123**, 136.
- 51 D. M. Moffatt, J. P. Runt, A. Halliayl and R. E. Newnham, *J. Mater. Sci.*, 1989, **24**, 609.
- 52 Y. Pan, G. Z. Wu and X. S. Yi, *J. Mater. Sci.*, 1994, **29**, 5757.
- 53 G. Van der Lee, B. Schuller, H. Post, T. L. F. Favre and V. Ponce, *J. Catal.*, 1986, **98**, 522.
- 54 C. Zheng, X. Zhang, S. He, Q. Fu and D. Lei, *J. Solid State Chem.*, 2003, **170**, 221.
- 55 K. Zhang, X. Sun, G. Lou, X. Liu, H. Li and Z. Su, *Mater. Lett.*, 2005, **59**, 2729.
- 56 Z. Yang, P. Cai, L. Chen, Y. Gu, L. Shi, A. Zhao and Y. Qian, *J. Alloys Compd.*, 2006, **420**, 229.
- 57 N. Pinna, M. Antonietti and M. Niederberger, *Colloids Surf., A*, 2004, **250**, 211.
- 58 S. A. Corr, M. Grossman, J. D. Furman, B. C. Melot, A. K. Cheetham, K. R. Heier and R. Seshadri, *Chem. Mater.*, 2008, **20**, 6396.
- 59 D. Munoz-Rojas and E. Baudrin, *Solid State Ionics*, 2007, **178**, 1268.
- 60 G. Anderson, *Acta Chem. Scand.*, 1956, **10**, 623.
- 61 A. D. Burton and P. A. Cox, *Philos. Mag.*, 1985, **51**, 255.
- 62 H. Liu, O. Vasquez, V. R. Santiago, L. Diaz and F. E. Fernandez, *J. Lumin.*, 2004, **108**, 233.
- 63 M. B. Sahana, G. N. Subbanna and S. A. Shivashankar, *J. Appl. Phys.*, 2002, **92**, 6495.
- 64 J. C. Rakotoniaina, R. Mokrani-Tamellin, J. R. Gavarrri, G. Vacquier, A. Casalot and G. Calvarin, *J. Solid State Chem.*, 1993, **103**, 81.
- 65 D. S. Su and R. Schloegl, *Catal. Lett.*, 2002, **83**, 115.
- 66 Y. Oka, T. Yao and N. Yamamoto, *J. Mater. Chem.*, 1991, **1**, 815.
- 67 G. T. Chandrappa, N. Steunou, S. Cassaignon, C. Bauvais and J. Livage, *Catal. Today*, 2003, **78**, 85.
- 68 Y. Mao and S. S. Wong, *J. Am. Chem. Soc.*, 2006, **128**, 8217.
- 69 Z. Gui, R. Fan, W. Mo, X. Chen, L. Yang, S. Zhang, Y. Hu, Z. Wang and W. Fan, *Chem. Mater.*, 2002, **14**, 5053.
- 70 C. Leroux, G. Nihoul and G. Van Tendeloo, *Phys. Rev. B*, 1998, **57**, 5111.
- 71 Y. Ueda, K. Kosuge and S. Kachi, *J. Solid State Chem.*, 1980, **31**, 171.
- 72 R. N. Bhowmik, R. Nagarajan and R. Ranganathan, *Phys. Rev. B*, 2004, **69**, 054430.
- 73 R. N. Bhowmik and R. Ranganathan, *Solid State Commun.*, 2007, **141**, 365.
- 74 J. Feinleib and W. Paul, *Phys. Rev.*, 1967, **155**, 841.
- 75 C. Grygiel, A. Pautrat, W. C. Sheets, W. Prellier, B. Mercey and L. Mechin, *J. Phys.: Condens. Matter*, 2008, **20**, 472205.